J. Fluid Mech. (2024), *vol*. 996, A49, doi:10.1017/jfm.2024.853

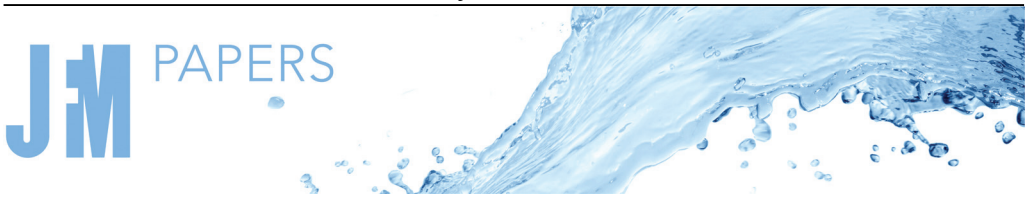

No sustained mean velocity in the boundary region of plane thermal convection

Roshan J. Samuel[1], **Mathis Bode**[2], **Janet D. Scheel**[3], **Katepalli R. Sreenivasan**[4,5,6] **and Jörg Schumacher**[1,4,†]

[1]Institute of Thermodynamics and Fluid Mechanics, Technische Universität Ilmenau, D-98684 Ilmenau, Germany

[2]Jülich Supercomputing Centre, Forschungszentrum Jülich GmbH, D-52425 Jülich, Germany

[3]Department of Physics, Occidental College, Los Angeles, CA 90041, USA

[4]Tandon School of Engineering, New York University, New York, NY 11201, USA

[5]Courant Institute of Mathematical Sciences, New York University, New York, NY 10012, USA

[6]Department of Physics, New York University, New York, NY 10012, USA

(Received 12 March 2024; revised 2 September 2024; accepted 2 September 2024)

We study the dynamics of thermal and momentum boundary regions in three-dimensional direct numerical simulations of Rayleigh–Bénard convection for the Rayleigh-number range $10^5 \leq Ra \leq 10^{11}$ and $Pr = 0.7$. Using a Cartesian slab with horizontal periodic boundary conditions and an aspect ratio of 4, we obtain statistical homogeneity in the horizontal x- and y-directions, thus approximating best an extended convection layer relevant for most geo- and astrophysical flow applications. We observe upon canonical use of combined long-time and area averages, with averaging periods of at least 100 free-fall times, that a global coherent mean flow is practically absent and that the magnitude of the velocity fluctuations is larger than the mean by up to 2 orders of magnitude. The velocity field close to the wall is a collection of differently oriented local shear-dominated flow patches interspersed by extensive shear-free incoherent regions which can be as large as the whole cross-section, unlike for a closed cylindrical convection cell of aspect ratio of the order 1. The incoherent regions occupy a 60 % area fraction for all Rayleigh numbers investigated here. Rather than resulting in a pronounced mean flow with small fluctuations about such a mean, as found in small-aspect-ratio convection, the velocity field is dominated by strong fluctuations of all three components around a non-existent or weak mean. We discuss the consequences of these observations for convection layers with larger aspect ratios, including boundary layer instabilities and the resulting turbulent heat transport.

Key words: Bénard convection

† Email address for correspondence: joerg.schumacher@tu-ilmenau.de

© The Author(s), 2024. Published by Cambridge University Press. This is an Open Access article, distributed under the terms of the Creative Commons Attribution licence (http://creativecommons.org/licenses/by/4.0), which permits unrestricted re-use, distribution and reproduction, provided the original article is properly cited.

https://doi.org/10.1017/jfm.2024.853 Published online by Cambridge University Press

1. Introduction

Rayleigh–Bénard convection (RBC) is one of the fundamental flow configurations in fluid turbulence research. The fluid in this configuration is nominally confined to an infinitely extended layer enclosed between two parallel, horizontal and impermeable plates separated by a vertical distance H (Rayleigh 1916). When the fluid layer is heated sufficiently strongly from below (and cooled from above), buoyancy forces initiate a turbulent fluid motion that has a statistically preferred state with respect to the direction of gravity, $\boldsymbol{g} = g\boldsymbol{e}_z$. A central question concerns the amount and nature of heat and momentum carried through the layer, and their dependencies on the imposed temperature difference between the top and bottom plates, $\Delta T = T_{bot} - T_{top}$. The temperature difference is expressed by the dimensionless Rayleigh number $Ra = g\alpha\Delta T H^3/(\nu\kappa)$, where α is the isobaric expansion coefficient, ν the kinematic viscosity and κ the temperature diffusivity (Ahlers, Grossmann & Lohse 2009*b*; Chillà & Schumacher 2012; Verma 2018).

A second important question is the structure of the velocity and thermal boundary layers on the horizontal walls and their effects on heat transport. Since the RBC system is enclosed by walls at the top and bottom, the viscous and thermal boundary layers formed on these walls pose a bottleneck for the global transport of both heat and momentum. Their composition and dynamics at very high Rayleigh numbers still need to be better understood, as emphasized recently (Iyer *et al.* 2020; Lindborg 2023; Shishkina & Lohse 2023; Creyssels & Martinard 2024). For Rayleigh numbers $Ra \gtrsim 10^{10}$, no laboratory experiment to date has resolved the dynamic interplay of the boundary layers and their fluctuations with the basic structural elements, namely thermal plumes and shear layers. Direct numerical simulations (DNS) are thus the only way to compare their structure and statistical properties with predictions from theories for canonical laminar and turbulent boundary layers (Schlichting & Gersten 2016). Furthermore, the closed-cell geometry of high-Rayleigh-number studies (Castaing *et al.* 1989; Chavanne *et al.* 1997; Niemela *et al.* 2000; Ahlers *et al.* 2009*a*; Urban *et al.* 2012) breaks the horizontal translation symmetry of the statistics, except possibly when the aspect ratio is very large (Pandey, Scheel & Schumacher 2018). Small aspect ratio enforces a dominant large-scale circulation (LSC) in the cell (Kadanoff 2001), manifesting as a relatively coherent shear flow connecting the top and bottom plates, fluctuating only moderately in its mean orientation (Sreenivasan, Bershadskii & Niemela 2002; Stevens, Lohse & Verzicco 2011; Shi, Emran & Schumacher 2012; Scheel & Schumacher 2017). Both aspects take us away from the original question on the heat and momentum transfer in an infinitely extended plane layer.

In this work, we focus more on the second question in a configuration that is closest to the original RBC model of convection between a pair of infinitely extended planes, by using periodic boundaries in both horizontal directions. Simulations with similar boundary conditions and Prandtl numbers have been done by Kerr (1996) for an aspect ratio $\Gamma = 6$ and $Ra \leq 2 \times 10^7$, by Hartlep, Tilgner & Busse (2003) for $\Gamma = 10$ and $Ra \leq 1 \times 10^7$, by van Reeuwijk, Jonker & Hanjalić (2008*a*) and van Reeuwijk, Jonker & Hanjalić (2008*b*) for $\Gamma = 4$ and $Ra \leq 1 \times 10^8$, by De, Eswaran & Mishra (2018) for $\Gamma = 6$ but $Ra \leq 2 \times 10^6$ and by Stevens *et al.* (2018) for $\Gamma \leq 32$ at $Ra = 10^9$. Our DNS span Rayleigh numbers of six orders of magnitude up to $Ra = 10^{11}$ for long periods of time (see table 1 for details). The choice of an aspect ratio of 4 for the present study provides a 'sweet spot'. On the one hand, the domain is large enough that it does not generate strong LSCs, see Niemela & Sreenivasan (2006). On the other hand, it is small enough to allow us to advance to very high Rayleigh numbers, here of up to $Ra = 10^{11}$, since the required numerical resources grow with Γ^2. Furthermore, this is the aspect ratio beyond which

https://doi.org/10.1017/jfm.2024.853 Published online by Cambridge University Press

Ra	Γ	N_e	p	N_{BL}	τ_{total}	Nu_{vol}	Nu_{wall}	Re	$Ra_{\delta,rms}$
10^5	4	$100 \times 100 \times 64$	5	71	1000	4.27 ± 0.24	4.27 ± 0.15	93.0 ± 2.6	104 ± 21
10^6	4	$100 \times 100 \times 64$	7	57	1000	8.15 ± 0.35	8.15 ± 0.19	296 ± 5	116 ± 14
10^7	4	$100 \times 100 \times 64$	9	42	1000	15.6 ± 0.9	15.6 ± 0.3	892 ± 17	144 ± 14
10^8	4	$150 \times 150 \times 96$	7	24	1000	30.4 ± 1.9	30.4 ± 0.4	2571 ± 47	174 ± 15
10^9	4	$150 \times 150 \times 96$	9	15	400	60.9 ± 4.4	60.8 ± 0.9	7300 ± 150	209 ± 15
$10^{9\,\dagger}$	2	$120 \times 120 \times 96$	9	21	100	62.4 ± 5.0	62.4 ± 1.2	6990 ± 210	177 ± 21
$10^{9\,\dagger}$	4	$220 \times 220 \times 96$	9	22	100	60.5 ± 3.8	60.5 ± 0.7	7340 ± 140	206 ± 18
$10^{9\,\dagger}$	8	$450 \times 450 \times 96$	9	22	100	60.9 ± 2.0	60.9 ± 0.3	7180 ± 70	212 ± 10
10^{10}	4	$400 \times 400 \times 200$	7	16	100	122.9 ± 10.8	123.1 ± 1.4	$20\,720 \pm 380$	247 ± 22
10^{11}	4	$500 \times 500 \times 256$	7	16	100	254 ± 21	253 ± 2	$58\,550 \pm 1040$	298 ± 23

Table 1. Details of the simulation series. Listed here are the Rayleigh number Ra, the aspect ratio Γ, the number of spectral elements N_e, the polynomial order p on each element with respect to each space direction, the number of collocation points within the thermal boundary layer N_{BL}, the total averaging time in free-fall units τ_{total}, the volume-averaged and wall-averaged Nusselt numbers, $Nu_{vol}(= Nu)$ and Nu_{wall}, the Reynolds number Re and the Rayleigh number based on the thermal fluctuation boundary layer thickness, $Ra_{\delta,rms}$. The three DNS runs with dagger symbols at $Ra = 10^9$ have a different vertical spectral element grid stretching than the fourth DNS run at this Rayleigh number. The total number of mesh cells is $N_e \times p^3$. It increases to almost 2.2×10^{10} collocation mesh cells for $Ra = 10^{11}$. Mean values in the last four columns are accompanied by the standard deviations. The Prandtl number of all runs is $Pr = 0.7$.

Nusselt and Reynolds numbers become independent of Γ, as discussed in Stevens *et al.* (2018). We supplement these results by additional DNS runs at $\Gamma = 2$ and 8 for $Ra = 10^9$.

A canonical mean-flow analysis reveals practically no global mean flow; instead, strong velocity fluctuations dominate the flow at all Ra. Fits to the mean vertical velocity profiles result in very small free-stream velocities $U_\infty \sim 10^{-3}$ in terms of the free-fall velocity $U_f = \sqrt{g\alpha\Delta TH}$, and thicknesses $\delta_\infty \sim 10^{-2}$ in terms of H, resulting in small shear Reynolds numbers $Re_{shear} \lesssim 1$–10 even for the largest Ra. We further analyse fluctuations of the velocity components, determine the distances of maximum mean-square fluctuations from the wall and discuss the resulting Reynolds numbers.

A quick impression of the complex boundary layer dynamics is obtained by the streamline and contour plots in figure 1 close to the bottom wall for two Rayleigh numbers. The figures indicate a prominent patchiness of the whole velocity boundary layer viewed from the top. The boundary layer is composed of coherent shear-dominated and incoherent shear-free regions. This feature becomes less prominent for the contours of the temperature field, which display an increasingly dense skeleton of thermal plume ridges over the whole plate. Here, we quantify the corresponding area fraction, condition the fluctuations on the coherent and incoherent regions and relate the incoherent regions to the large-scale patterns in the bulk, which are the turbulent superstructures of convection (Pandey *et al.* 2018; Stevens *et al.* 2018). Only when the velocity fluctuations are conditioned on the coherent shear-dominated regions are the mean profiles close to those observed in closed cylinders for $\Gamma \sim 1$ (Scheel & Schumacher 2017).

One important point needs to be made here. While a thermal boundary layer of the standard type is indeed present, no momentum boundary layer can be easily identified, as explained subsequently. For the velocity field, it is thus more accurate to merely discuss the flow near the wall instead of the boundary layer flow, but for convenience of identification and following convention, we continue to use the term boundary layer. There is no such ambiguity for the thermal boundary layer.

https://doi.org/10.1017/jfm.2024.853 Published online by Cambridge University Press

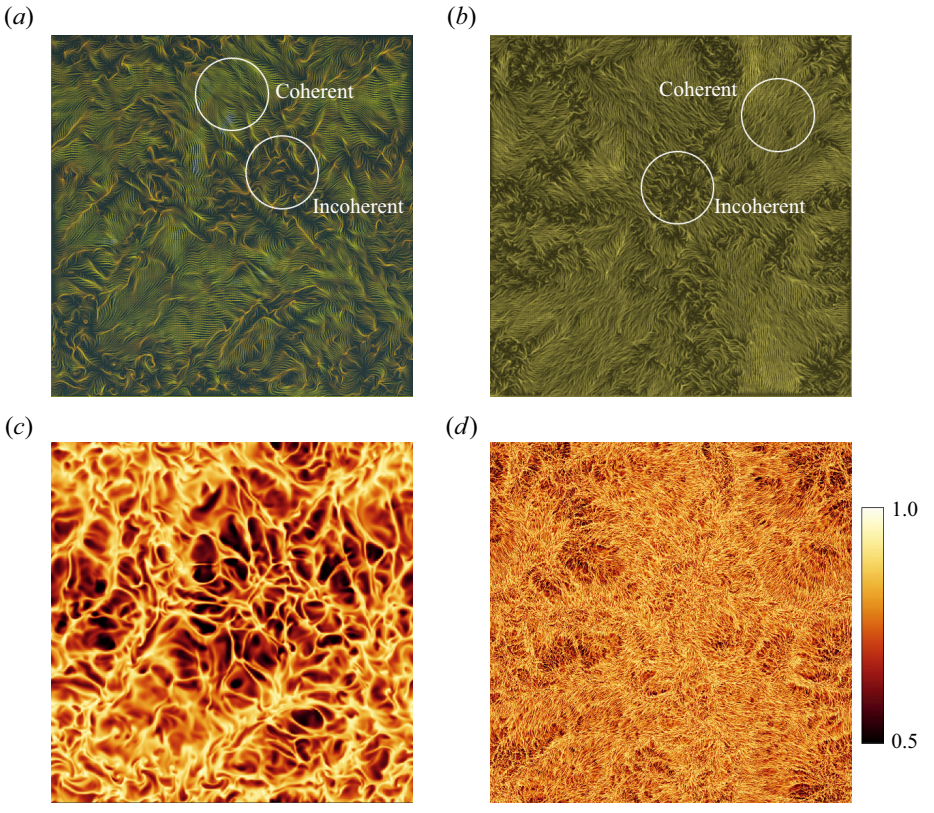

Figure 1. Turbulent fields at two Rayleigh numbers. Streamline snapshots of the horizontal velocity field (u_x, u_y) and contour plots of temperature field T at the same instant. Panels show (*a*,*c*) $Ra = 10^8$ and (*b*,*d*) $Ra = 10^{11}$. The entire cross-section of $4H \times 4H$ at $z = \delta_T/2$ close to the bottom wall is shown. Here, H is the height of the convection layer and δ_T the thermal boundary layer thickness. The colour legend holds for both temperature field panels (*c*,*d*). In panels (*a*,*b*) examples for local coherent shear-dominated and incoherent shear-free regions are indicated.

2. Numerical simulations and resolution analysis

We solve the three-dimensional Boussinesq equations of RBC (Verma 2018) by the GPU-based spectral element code nekRS (Fischer *et al.* 2022) which combines an element decomposition of the computational domain with a spectral expansion in Lagrange polynomials of each involved field along each spatial dimension on each element. The equations are given in dimensionless form by

$$\frac{\partial \boldsymbol{u}}{\partial t} + (\boldsymbol{u}\cdot\boldsymbol{\nabla})\boldsymbol{u} = -\boldsymbol{\nabla} p + T\hat{\boldsymbol{z}} + \sqrt{\frac{Pr}{Ra}}\,\nabla^2\boldsymbol{u}, \tag{2.1}$$

$$\frac{\partial T}{\partial t} + (\boldsymbol{u}\cdot\boldsymbol{\nabla})T = \frac{1}{\sqrt{PrRa}}\,\nabla^2 T, \tag{2.2}$$

$$\boldsymbol{\nabla}\cdot\boldsymbol{u} = 0. \tag{2.3}$$

Here, $\boldsymbol{u}$, p and T are the velocity, pressure and temperature fields, respectively. Length, velocity and temperature are expressed in units of H, U_f and the outer temperature difference ΔT, respectively. No-slip boundary conditions apply for the velocity field at the plates at $z = 0$ and H. Table 1 summarizes 10 simulations, all at a Prandtl number

https://doi.org/10.1017/jfm.2024.853 Published online by Cambridge University Press

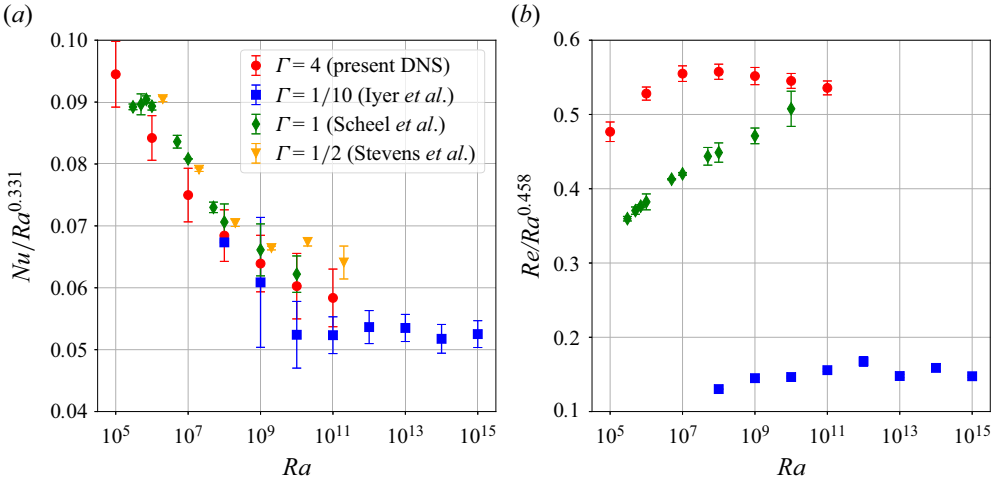

Figure 2. (*a*) Compensated turbulent heat transfer $Nu/Ra^{0.331}$ vs Ra. (*b*) Compensated turbulent momentum transfer $Re/Ra^{0.458}$ vs Ra. The panels contain data from the present DNS and from Scheel & Schumacher (2017), Stevens *et al.* (2010) and Iyer *et al.* (2020). All data are compensated by the fits to the data from Iyer *et al.* (2020); see also table 1.

$Pr = \nu/\kappa = 0.7$ and aspect ratios $\Gamma = L/H = 2$, 4 and 8, where L is the horizontal length. The number of collocation points inside the thermal boundary layer (based on the temperature fluctuation profiles) is always $N_{BL} \geq 15$. Furthermore, we verified that the Nusselt numbers Nu_{vol} and Nu_{wall}, which are given by combined volume–time $\langle\cdot\rangle_{V,t}$ and area–time averages $\langle\cdot\rangle_{A,t}$,

$$Nu_{vol} = 1 + \sqrt{RaPr}\langle u_z T\rangle_{V,t} \quad \text{and} \quad Nu_{wall} = -\frac{\partial\langle T\rangle_{A,t}}{\partial z}\bigg|_{z=0,H}, \tag{2.4a,b}$$

result in practically the same values (table 1).

As a first global result, we plot in figure 2(*a*,*b*) the Nusselt and Reynolds numbers, $Nu = Nu_{vol}$ and $Re = U_{rms}\sqrt{Ra/Pr}$ vs the Rayleigh number Ra, compensated by the high-Ra scaling result of Iyer *et al.* (2020); here, $U_{rms} = \langle \boldsymbol{u}^2\rangle_{V,t}^{1/2}$ is the root-mean-square velocity. Also compared are our results with those of Stevens, Verzicco & Lohse (2010) and Scheel & Schumacher (2017) in closed cylinders at $\Gamma = 1/2$ and $\Gamma = 1$, respectively. Considering the large differences in aspect ratios, the Nusselt numbers collapse fairly well and follow the same trend for $Ra \leq 10^{11}$ (figure 2*a*); they are also in agreement with previous simulations for $Ra \leq 10^8$ from van Reeuwijk *et al.* (2008*a*). The Reynolds number shows a strong geometry dependence, as visible in figure 2(*b*), although they tend to the same exponent towards high Ra; this suggests an agreement in scaling exponents at high Ra, but the prefactor seems to have a complicated Rayleigh-number dependence. Statistics in all runs are obtained for equal and more than 100 free-fall times $T_f = H/U_f$; see table 1.

We verified that the resolution of the boundary layers is sufficient. Figure 3 shows the vertical profiles of the temperature fluctuations for three different spectral element grids at $Ra = 10^{10}$ and two at $Ra = 10^{11}$ with different polynomial orders $p \geq 5$. It is seen that the profiles collapse well on each other, thus also demonstrating the convergence of the spectral method. This conclusion is further reinforced for $Ra = 10^9$ where we have 4 DNS runs at different aspect ratio and vertical grid stretching. First, the Nusselt and Reynolds

https://doi.org/10.1017/jfm.2024.853 Published online by Cambridge University Press

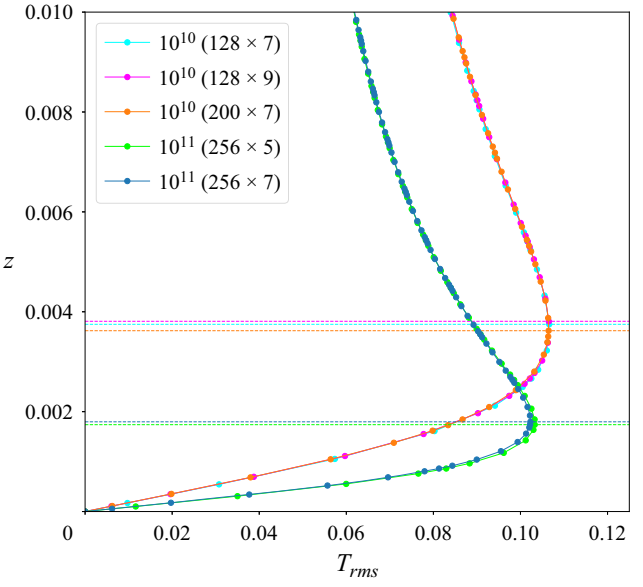

Figure 3. Resolution study for the runs at the two highest Rayleigh numbers. The near-wall profile of the temperature fluctuations is plotted. The legend indicates the Rayleigh number together with the vertical numbers of spectral elements and the polynomial order. The runs, as listed in the legend from top to bottom, have 11, 14, 16, 11 and 16 points inside the thermal boundary layer. The horizontal lines are the thermal fluctuation boundary layer thicknesses.

numbers in table 1 differ only slightly (of the order of a tenth of a per cent) between $\Gamma = 4$ and 8. Secondly, they are very close for two element grids with different vertical grid stretching at $\Gamma = 4$. The fast spectral convergence of spectral element methods in comparison with lower-order finite-difference schemes has been reported recently by Zahtila *et al.* (2023) in comprehensive studies for turbulent channel flows.

3. Mean profiles of temperature and velocity

The mean velocity profiles for the horizontal components are obtained by a combined average over the area $A = L^2$ and $N_t = 20$ statistically independent realizations of the turbulent flow separated from each other by at least $5T_f$ as

$$\langle u_i \rangle_{A,t}(z) = \frac{1}{AN_t} \sum_{k=1}^{N_t} \int_A u_i(x, y, z, t_k)\, \mathrm{d}A, \tag{3.1}$$

for $i = x, y$ and N_t the number of snapshots. For all runs, $N_t = 20$ to obtain equidistant and statistically independent realizations of the flow. Figure 4 displays the result of this analysis for $Ra = 10^9$. In panel (*a*), the mean profile of the x-velocity component is shown as a function of even longer averaging times, which were varied from $\tau_{total} = 400\,T_f$ (= 20 snapshots) to $1600\,T_f$ (= 80 snapshots). The profile converges steadily to zero, although not uniformly. There is essentially no mean flow. If we insist upon fitting the near-wall mean profiles to the two-dimensional Blasius solution, for example, the result is shown in panel (*b*). In the absence of a definable leading edge distance x, we match $\langle u_x \rangle_{A,t}(z)/U_\infty$ and z/δ_∞ to $f'(\eta)$ which is reported in panels (*b*,*c*) of figure 4. Recall that the Blasius solution $f(\eta) = \psi(x, z)/\sqrt{xU_\infty \nu}$ and $\eta = z/\delta(x)$ (Schlichting & Gersten 2016),

https://doi.org/10.1017/jfm.2024.853 Published online by Cambridge University Press

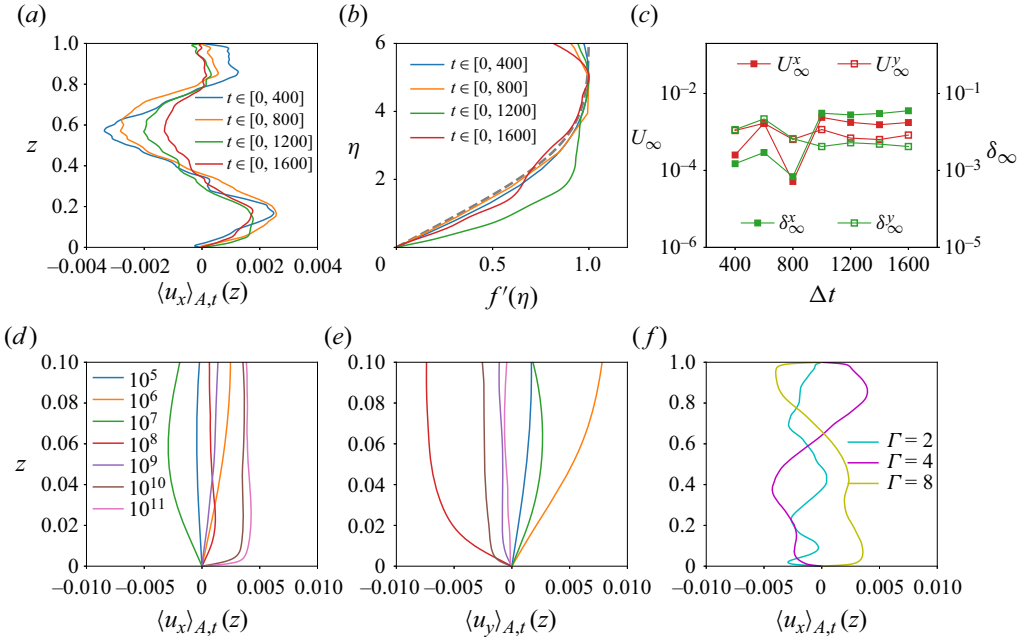

Figure 4. (*a*) Planar-averaged profiles of the horizontal velocity component u_x for different averaging intervals for $Ra = 10^9$. Notice the very small values of U_∞ and the non-monotonic convergence of the profiles. (*b*) Match of the near-wall profiles from panel (*a*) to the Blasius profile $f'(\eta)$ (dashed line). (*c*) Variation of the free-stream velocity U_∞ and boundary layer height δ_∞ obtained from the fits to the Blasius profile vs averaging time at $Ra = 10^9$. (*d*) Time-averaged profiles $\langle u_x \rangle_{A,t}$ for all 7 Rayleigh numbers. (*e*) Time-averaged profiles $\langle u_y \rangle_{A,t}$ for all 7 Rayleigh numbers. (*f*) Time-averaged profiles $\langle u_x \rangle_{A,t}$ for Rayleigh number $Ra = 10^9$ and aspect ratios $\Gamma = 2$, 4 and 8. These are the three runs which are indicated by a dagger in table 1.

where $\psi(x, z)$ is the streamfunction and $u_x = \partial\psi/\partial z$ and $u_z = -\partial\psi/\partial x$. The numerical profiles are rescaled such that the first local maximum of $\langle u_x \rangle_{A,t}$ corresponds to U_∞. The fits are shown for different time intervals in (*b*). Recall that, at distance $\eta = 5$, the Blasius profile reaches a streamwise velocity magnitude of $f'(\eta) = 0.99U_\infty$. In this case, panel (*a*) shows that the maximum velocity reached is of the order 1 % or less of the free-fall velocity, which is the only characteristic velocity of the flow. As shown in panel (*c*), no clear trend of the velocity $U_\infty^{x,y}$ with averaging time is detectable, and the magnitude is between $O(10^{-3})$ and $O(10^{-2})$. In table 2, the results for all Rayleigh numbers and both horizontal components are listed.

The boundary layer thickness parameters vary when x- and y-directions are compared at fixed Ra. They decrease with increasing Rayleigh number. Furthermore, we calculate the corresponding shear Reynolds numbers $Re_{shear} = U_\infty \delta_\infty / \nu$, which are found to be very small for all cases. Panels (*d*,*e*) of figure 4 show the mean profiles for all 7 simulation runs and for both horizontal velocity components. They underline the very small mean-flow amplitudes for all Rayleigh numbers in this series. Panel (*f*) of the figure compares three runs at $Ra = 10^9$, which are indicated with a dagger symbol in table 1, at aspect ratios $\Gamma = 2$, 4 and 8. Again, the mean-flow amplitudes $\langle u_x \rangle_{A,t}(z)$ are comparable and very small such that an aspect-ratio dependence for this result can be excluded when periodic boundary conditions in the horizontal directions are applied. The non-monotonic behaviour is simply a reflection of the long averaging times required for convergence in convection studies.

https://doi.org/10.1017/jfm.2024.853 Published online by Cambridge University Press

Ra	U^x_∞	U^y_∞	δ^x_∞	δ^y_∞	Re^x_{shear}	Re^y_{shear}
10^5	4.8×10^{-4}	1.7×10^{-3}	9.1×10^{-1}	6.5×10^{-1}	0.16	0.43
10^6	2.5×10^{-3}	8.4×10^{-3}	1.7×10^{-1}	1.5×10^{-1}	0.51	1.5
10^7	3.0×10^{-3}	2.7×10^{-3}	8.2×10^{-2}	8.1×10^{-2}	0.93	0.82
10^8	1.2×10^{-3}	6.6×10^{-3}	5.8×10^{-2}	3.7×10^{-2}	0.80	2.9
10^9	2.5×10^{-4}	9.3×10^{-4}	5.1×10^{-2}	2.7×10^{-2}	0.48	0.94
10^{10}	3.3×10^{-3}	1.8×10^{-3}	1.3×10^{-2}	1.1×10^{-2}	5.1	2.4
10^{11}	3.6×10^{-3}	1.4×10^{-4}	5.8×10^{-3}	7.0×10^{-3}	7.9	0.38

Table 2. Fit parameters U^x_∞ and U^y_∞ as well as the corresponding thicknesses δ^x_∞ and δ^y_∞ of the combined plane–time-averaged mean profiles of the horizontal velocity components $\langle u_x\rangle_{A,t}$ and $\langle u_y\rangle_{A,t}$ to the Blasius profile $U_\infty f'(\eta)$ with $\eta = z/\delta_\infty$. The corresponding shear Reynolds numbers $Re^{x,y}_{shear} = U^{x,y}_\infty \delta^{x,y}_\infty/\nu$ are also given. All runs are at $\Gamma = 4$.

4. Fluctuation profiles of temperature and velocity

The mean vertical profiles of the root-mean-square velocities are given by

$$U^h_{rms}(z) = \sqrt{\langle u_x^2 + u_y^2\rangle_{A,t}} \quad \text{and} \quad U_{rms}(z) = \sqrt{\langle u_x^2 + u_y^2 + u_z^2\rangle_{A,t}}, \tag{4.1a,b}$$

where we distinguish between horizontal and full profiles. The fluctuation profiles for the velocity fields are obtained from the full components since the means are so small. We have verified that the differences in the procedure produce only very small changes. Figure 5 summarizes mean profiles for 7 simulation runs, the mean temperature profile and the root-mean-square profiles of temperature, horizontal velocity components and all three velocity components. The temperature fluctuation profile is similarly obtained by $T_{rms}(z) = \langle\theta^2\rangle^{1/2}_{A,t}$ with $\theta(\boldsymbol{x}, t) = T(\boldsymbol{x}, t) - \langle T\rangle_{A,t}(z)$. The corresponding characteristic scales are indicated by horizontal dashed lines and detailed in table 3. It is seen that the thermal boundary layer thickness $\delta_T = 1/(2Nu)$ is slightly larger than the distance from the wall of the maximum of the temperature fluctuation profile, which we term the thermal fluctuation boundary layer thickness or, for short, thermal fluctuation thickness, $\delta_{T,rms}$. Increasingly larger are distances from the wall to the maxima of the velocity fluctuation profiles, obeying a ratio of $\delta_{U,rms}/\delta_{T,rms} \approx 2$ for $Ra = 10^5$ up to approximately 13 for $Ra = 10^{11}$; see panel (*d*). The corresponding thicknesses are termed velocity fluctuation thickness.

Furthermore, we repeated the fluctuation profile analysis for the dependence on different aspect ratios, one on each side of 4, at $Ra = 10^9$. These runs are indicated again by a dagger symbol in table 3, where we collect the corresponding thickness scales. The corresponding profiles are shown in figure 6. While the temperature profiles collapse close to the walls, thus displaying no sensitivity with respect to the aspect ratio Γ in this range, the velocity profiles are affected by Γ. However, the resulting velocity fluctuation thicknesses are found to agree well for $\Gamma = 4$ and 8 (by 1.5 % or less), in terms of both horizontal and full velocity fluctuations. The finding supports our considered view that $\Gamma \geq 4$ is sufficient to obtain horizontal homogeneity for the statistics already introduced.

5. Scaling of combined volume–time-averaged fluctuation with Rayleigh number

Figure 7 summarizes the root-mean-square fluctuations of the three velocity components and the temperature. They are obtained by a combined average with respect to the full

https://doi.org/10.1017/jfm.2024.853 Published online by Cambridge University Press

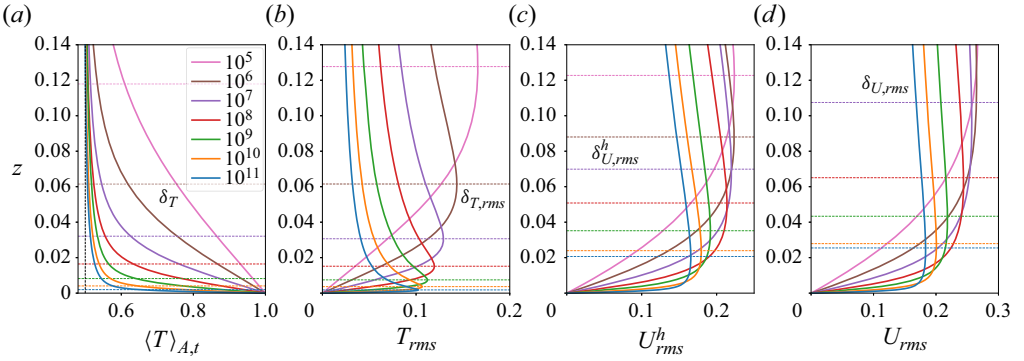

Figure 5. Mean profiles are compared with each other for all 7 runs. We show the mean profile of temperature $\langle T\rangle_{A,t}(z)$ in panel (*a*), root-mean-square profile of temperature $T_{rms}(z)$ in (*b*), root-mean-square profile with respect to the two horizontal velocity components, $U^h_{rms}(z)$, in (*c*) and with respect to all three components, $U_{rms}(z)$, in (*d*). The corresponding height scales of these profiles are indicated by dashed horizontal lines in the figures and listed in table 3. Note that, for the two lowest *Ra*, they exceed the displayed plot range of the figure in panel (*d*).

Ra	Γ	δ_T	$\delta_{T,rms}$	$\delta^h_{U,rms}$	$\delta_{U,rms}$
10^5	4	$(1.17 \pm 0.04) \times 10^{-1}$	$(1.27 \pm 0.08) \times 10^{-1}$	$(1.23 \pm 0.07) \times 10^{-1}$	$(2.39 \pm 1.32) \times 10^{-1}$
10^6	4	$(6.13 \pm 0.15) \times 10^{-2}$	$(6.13 \pm 0.27) \times 10^{-2}$	$(8.80 \pm 0.54) \times 10^{-2}$	$(1.74 \pm 1.12) \times 10^{-1}$
10^7	4	$(3.21 \pm 0.06) \times 10^{-2}$	$(3.07 \pm 0.10) \times 10^{-2}$	$(6.99 \pm 0.58) \times 10^{-2}$	$(1.07 \pm 0.51) \times 10^{-1}$
10^8	4	$(1.64 \pm 0.02) \times 10^{-2}$	$(1.52 \pm 0.04) \times 10^{-2}$	$(5.08 \pm 0.35) \times 10^{-2}$	$(6.51 \pm 0.92) \times 10^{-2}$
10^9	4	$(8.22 \pm 0.12) \times 10^{-3}$	$(7.47 \pm 0.18) \times 10^{-3}$	$(3.52 \pm 0.28) \times 10^{-2}$	$(4.33 \pm 1.97) \times 10^{-2}$
$10^{9\,\dagger}$	2	$(8.01 \pm 0.15) \times 10^{-3}$	$(7.07 \pm 0.29) \times 10^{-3}$	$(2.94 \pm 0.49) \times 10^{-2}$	$(3.75 \pm 0.72) \times 10^{-2}$
$10^{9\,\dagger}$	4	$(8.27 \pm 0.10) \times 10^{-3}$	$(7.44 \pm 0.21) \times 10^{-3}$	$(3.28 \pm 0.28) \times 10^{-2}$	$(4.15 \pm 0.63) \times 10^{-2}$
$10^{9\,\dagger}$	8	$(8.20 \pm 0.04) \times 10^{-3}$	$(7.51 \pm 0.12) \times 10^{-3}$	$(3.23 \pm 0.12) \times 10^{-2}$	$(4.20 \pm 0.22) \times 10^{-2}$
10^{10}	4	$(4.06 \pm 0.04) \times 10^{-3}$	$(3.67 \pm 0.11) \times 10^{-3}$	$(2.39 \pm 0.19) \times 10^{-2}$	$(2.79 \pm 0.27) \times 10^{-2}$
10^{11}	4	$(1.97 \pm 0.02) \times 10^{-3}$	$(1.81 \pm 0.05) \times 10^{-3}$	$(2.07 \pm 0.27) \times 10^{-2}$	$(2.55 \pm 0.39) \times 10^{-2}$

Table 3. Differently defined boundary layer thicknesses of temperature and velocity according to the vertical mean profiles plotted in figure 5. The standard deviation accompanies each mean value.

volume $V = L^2H$ and time, e.g. $u_{x,rms} = \langle u_x^2\rangle^{1/2}_{V,t}$. The quantity U_{rms} denotes again the fluctuations with respect to all three velocity components. It is seen that the dependence of the velocity fluctuations on the Rayleigh number is very weak with $\beta \lesssim 0.042$. The temperature fluctuations drop with a smaller power-law exponent, $T_{rms} \sim Ra^{-\beta}$, which is found to be $\beta = 0.119$ for the present data. This exponent is slightly smaller in magnitude than those reported in experiments in cylindrical cells of aspect ratio 1/2. For comparison, Castaing *et al.* (1989), Niemela *et al.* (2000) and Wu & Libchaber (1992) report exponents of $\beta \approx 0.145$. We also analysed the temperature fluctuations in the bulk of the layer, which takes a volume average with respect to $V_b = L^2 \times [0.4, 0.6]$ and time. The exponent changes to $\beta = 0.141$ which is closer to the experiments. We have verified that a variation of the thickness of the bulk volume V_b does not alter the results significantly.

In panels (*b–d*) of figure 7, we added data from the DNS of Iyer *et al.* (2020) for comparison, which were obtained in a closed slender cylindrical cell of aspect ratio $\Gamma = 0.1$. It is seen that exponents of the power-law fits are close to those of the present simulation series. The prefactors differ as expected, because the former DNS data were

https://doi.org/10.1017/jfm.2024.853 Published online by Cambridge University Press

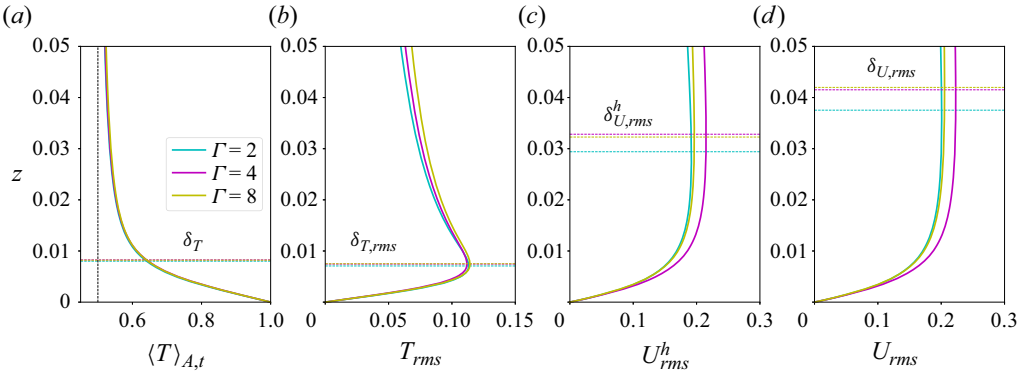

Figure 6. Mean temperature profiles compared with each other for different aspect ratios at $Ra = 10^9$. Similar to figure 5, we show the mean profile of temperature $\langle T\rangle_{A,t}(z)$ in panel (a), root-mean-square profile of temperature $T_{rms}(z)$ in (b), root-mean-square profile with respect to the horizontal velocity components, $U^h_{rms}(z)$ in (c) and with respect to all three components $U_{rms}(z)$ in (d). The corresponding height scales of these profiles are indicated by dashed horizontal lines and are also listed in table 3.

obtained for geometrically constrained convection. This finding of nearly the same scaling exponents suggests a robust geometry-independent trend of all thermal fluctuations with respect to the Rayleigh number. Geometry-specific aspects mostly affect the prefactor.

6. Decomposition into coherent and incoherent boundary layer regions

The orientation of the boundary layer flow varies strongly, as shown in figures 8(a) and 8(c), where we plot the orientation angle of the horizontal velocity $\varphi = \arctan(u_y/u_x) \in [-\pi, \pi]$ for a snapshot at $Ra = 10^{10}$ at $z = \delta_T$ and $z = H - \delta_T$, respectively. At both these heights, we cover the horizontal plane into 10^4 disjoint square boxes of area content $A_i = A/10^4$, where $A = L^2$. We then calculate the mean horizontal velocity $\bar{\boldsymbol{u}}_h(A_i)$ in each of A_i and decompose the cross-section into coherent and incoherent boundary layer regions for $|\bar{\boldsymbol{u}}_h(A_i)| > U^h_{rms}(\delta_T)$ and $|\bar{\boldsymbol{u}}_h(A_i)| \leq U^h_{rms}(\delta_T)$, respectively. Similar decompositions have been applied to analyse the spatio-temporal intermittency of the transition to turbulence in shear flow turbulence in extended domains, see e.g. Hof (2022). Panels (a,c) of figure 8 show that coherent shear-dominated patches are separated by incoherent flow regions (in grey). See also figure 1. The superposed streamlines indicate the different flow orientations of the shear-dominated regions.

Panels (b,d) of the same figure show the corresponding snapshots of the temperature field T at $z = 0.1$ above the bottom and $z = 0.9$ below the top, which are distances of 25 δ_T away from the walls at $Ra = 10^{10}$. It is clearly seen that the hotter regions at $z = 0.1$ and the colder regions at $z = 0.9$, both of which are displayed in grey, coincide fairly well with the incoherent flow regions at the edge of the thermal boundary layer. We can define overlap factors $0 \leq \tilde{O} \leq 1$ by

$$\tilde{O}_{bot} = \frac{A_{incoh} \bigcup A_{T>T_0}}{\max(A_{incoh}, A_{T>T_0})} \quad \text{and} \quad \tilde{O}_{top} = \frac{A_{incoh} \bigcup A_{T<T_0}}{\max(A_{incoh}, A_{T<T_0})}, \tag{6.1a,b}$$

with $T_0 = 0.5$. Here, we find mean overlaps of $\langle\tilde{O}_{bot}\rangle = 0.60$ and $\langle\tilde{O}_{top}\rangle = 0.63$, where the average is taken over the snapshots. The physical interpretation is as follows: the incoherent regions correspond to dominant hotter upwelling (colder downwelling) motions. These regions occur outside shear-dominated patches where the thermal plumes

https://doi.org/10.1017/jfm.2024.853 Published online by Cambridge University Press

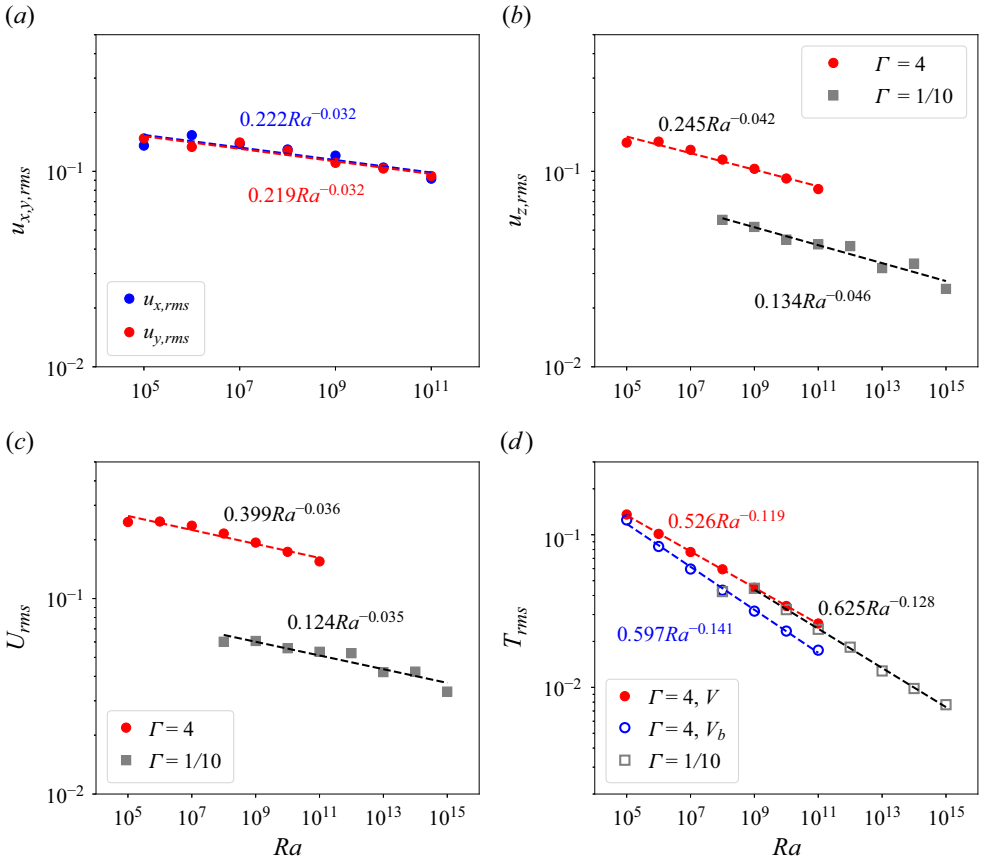

Figure 7. Scaling of the root-mean-square velocities and temperature with respect to Rayleigh number. All values are obtained by a combined average with respect to volume and time. (*a*) Horizontal velocity components. (*b*) Vertical velocity component. (*c*) All three velocity components. (*d*) Temperature. Dashed lines denote power-law fits to the data. Blue open circles stand for data obtained in the bulk volume V_b. In panels (*b–d*), we add data from Iyer *et al.* (2020) with separate fits. The corresponding temperature data are obtained there for the cylindrical cell interior, $r \leq 0.03H$ and $Ra \geq 10^9$.

merge successively with growing distances from the walls. As one approaches the mid-plane of the convection cell, they tend to form the turbulent superstructure pattern of convection. We have determined that the area fraction of the incoherent regions remains nearly constant at approximately 60 % of A for the whole Rayleigh-number range. The insensitivity of the volume fractions with respect to the Rayleigh number suggests that this skeleton of upwelling (downwelling) incoherent regions could be a relic from the weakly nonlinear regime of convection at much lower Rayleigh numbers, which itself arises from the onset of convection by a linear primary instability, filling the whole domain with convection rolls.

We have varied the threshold for this analysis from $0.5U^h_{rms}(\delta_T)$ to $2U^h_{rms}(\delta_T)$. While the incoherent fractions do depend on the threshold when its variations are large, they are practically independent of the Rayleigh number even for such large variations stated above. This supports our choice of $U^h_{rms}(\delta_T)$ as a physically meaningful threshold.

We can now return to the fluctuation analysis which is conditioned on coherent and incoherent regions in the following. Figure 9 replots the root-mean-square profiles of full

https://doi.org/10.1017/jfm.2024.853 Published online by Cambridge University Press

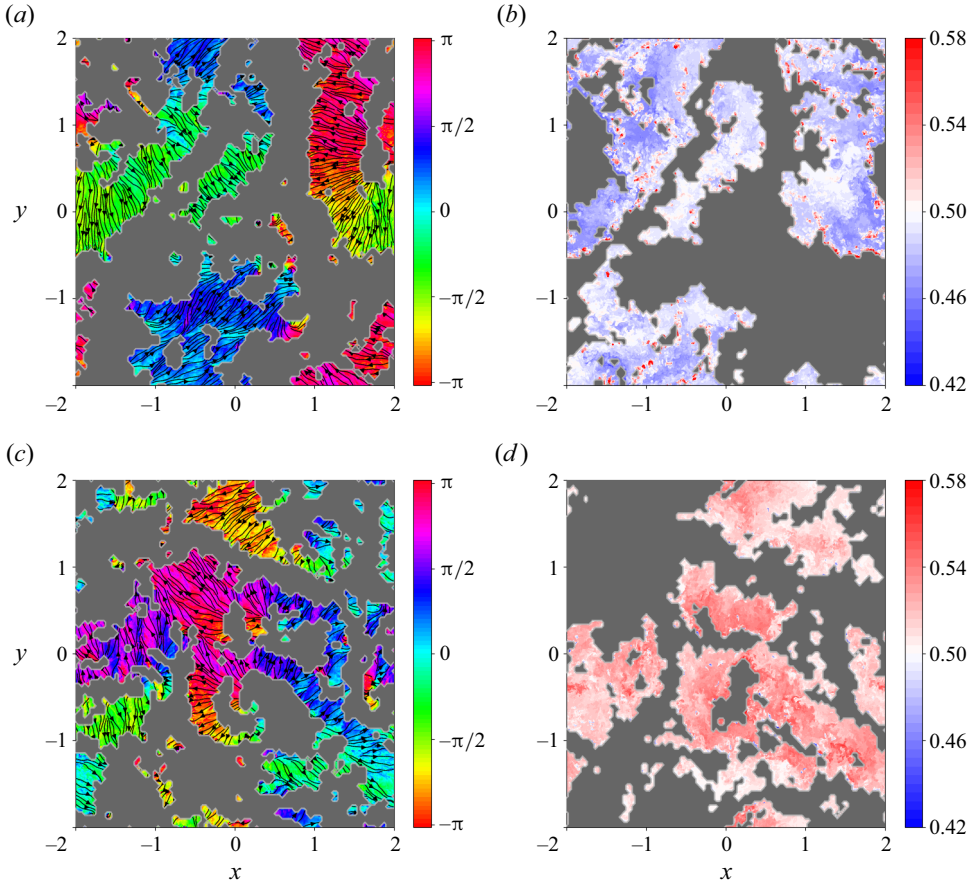

Figure 8. Boundary layer flow structure for $Ra = 10^{10}$ at the top and bottom walls. (*a*) Decomposition of a snapshot into coherent and incoherent (in grey) flow regions at $z = \delta_T$. For the coherent shear-dominated regions, we overlay horizontal streamlines and indicate their local flow direction. (*b*) Corresponding temperature field in plane at $z = 0.1 \approx 25\delta_T$. Grey area corresponds to $T > T_0 = 0.5$. (*c*) Same snapshot with the decomposition similar to (*b*) for $z = H - \delta_T$ close to the top wall. (*d*) Corresponding temperature field at $z = 0.9 \approx 25\delta_T$. Grey area corresponds now to $T < T_0$. Note that all plots are shown at the coarse resolution of 100×100 square boxes (which were used to calculate the local mean-flow magnitude and orientation) and not at the original spectral resolution of the DNS run.

and horizontal velocity and temperature profiles for Rayleigh numbers $Ra = 10^8$, 10^9 and 10^{10}. We have chosen these three Rayleigh numbers of our series to provide a one-to-one comparison with DNS data in a closed cylindrical cell at $\Gamma = 1$ of Scheel & Schumacher (2017). They are also shown in the figure. Vertical profiles, which have been taken over the full cross-section (denoted as case G4 in the following), are shown in the left column of figure 9. Profiles conditioned on shear-dominated regions are displayed in the middle column (case G4C), while those for the cylindrical cross-section of the closed container (case G1) are shown in the right column. From the bottom row of the figure, it is clear that the temperature profiles of G4, G4C and G1 for all three *Ra* agree. This suggests that the temperature boundary layers are alike in all cases. This is different for the velocity field, for which the horizontal velocity fluctuations (displayed in top row) show a clear trend. The thickness scale decreases from G4 to G4C and even more from G4C to G1.

https://doi.org/10.1017/jfm.2024.853 Published online by Cambridge University Press

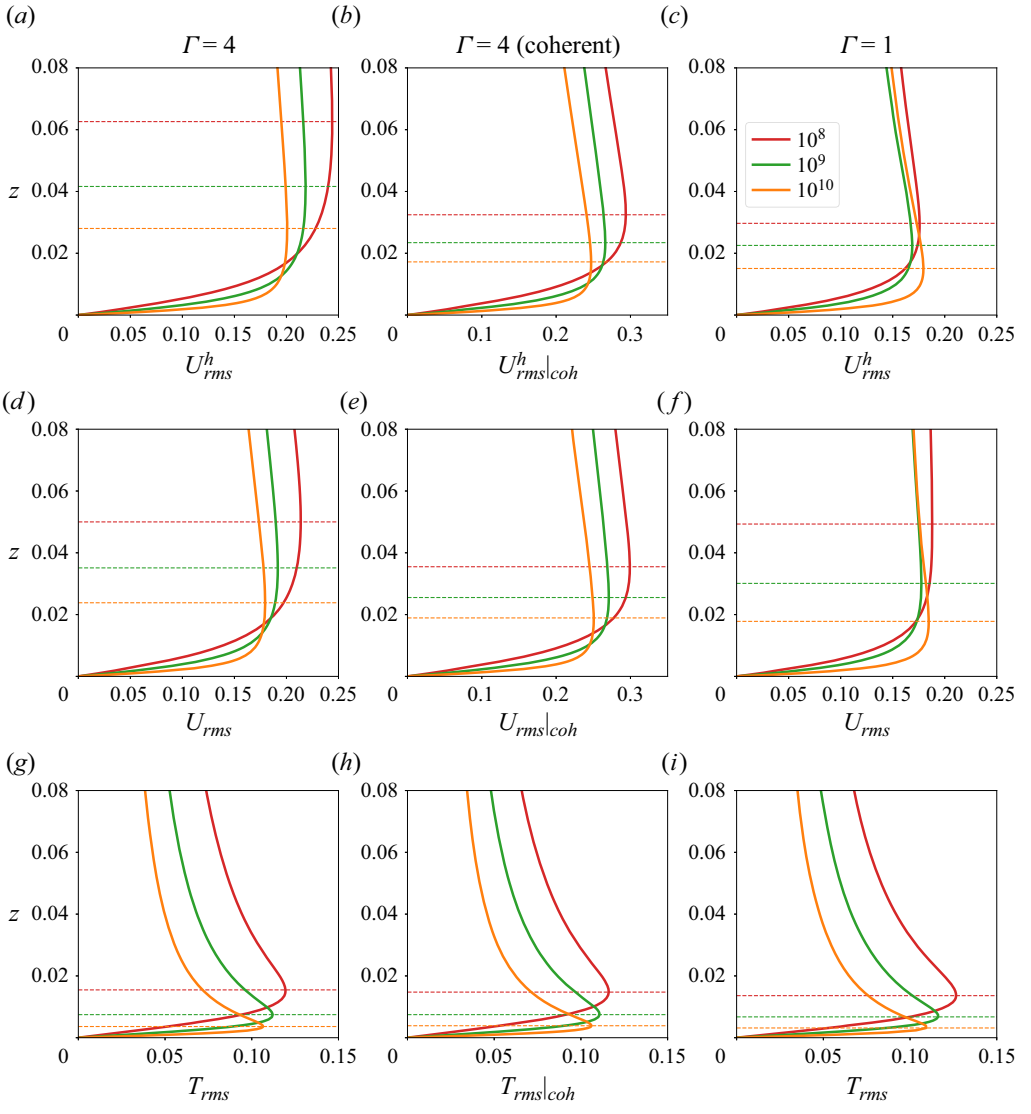

Figure 9. Vertical profiles of the velocity and temperature fluctuations for Rayleigh numbers $Ra = 10^8$, 10^9 and 10^{10}. The figure compares averages over the full cross-section at $\Gamma = 4$ (*a*,*d*,*g*) with averages over the coherent shear-dominated regions (*b*,*e*,*h*) and with averages over the full circular cross-section in a closed cylindrical cell at $\Gamma = 1$ (*c*,*f*,*i*) from Scheel & Schumacher (2017). Panels (*a*–*c*) are for U^h_{rms}, panels (*d*–*f*) for U_{rms} and panels (*g*–*i*) for T_{rms}. The dashed lines in each panel mark the location of the first local maximum away from the wall, and indicate the corresponding fluctuation thickness. The colour coding, which is indicated in panel (*c*), holds for all panels.

The close agreement of G4C and G1 clearly supports the dominance of shearing motion in the boundary regions in closed cylindrical cells, imposed by the prominent LSC. It is in line with a reduced fluctuation thickness. For fluctuations with respect to the full velocity field, we do detect a decrease of the thickness from G4 to G4C, but not from G4C to G1 for the two lower *Ra*. We suspect that this might be caused by prominent coherent up- and downwelling motions at the sidewalls for the lower *Ra* which effectively enhance the thickness (Schumacher & Scheel 2016).

https://doi.org/10.1017/jfm.2024.853 Published online by Cambridge University Press

Unlike G1 and G4C, for which the velocity and temperature boundary layers have comparable thicknesses, the G4 case shows that the velocity boundary layer is much thicker than the temperature thickness, suggesting a different mechanism in G4. We recall that the notion of the velocity boundary layer is only nominal in the sense that they are based on fluctuation profiles and the mean velocity variation within that region is quite small (see figure 4).

7. Final discussion

Our DNS of the turbulent Rayleigh–Bénard convection encompass a Cartesian domain with $\Gamma = 4$, with no-slip horizontal walls and periodic boundary conditions for the side faces. These simulations of up to $Ra = 10^{11}$ are aimed at approaching the original canonical case of a plane convection layer between a pair of infinitely extended rigid plates. We demonstrated that a standard mean-flow profile (obtained by combining averages with respect to time and the entire horizontal cross-sectional plane) have very small magnitudes, and that efforts to match them to laminar boundary layer profiles produced no conclusive results. To the extent that we can define the boundary layers, they give very small shear Reynolds numbers (see below). In the long-time limit, which we have followed for 1600 T_f at $Ra = 10^9$, the velocity mean profiles have to converge to $\lim_{t\to\infty}\langle u_i\rangle_{A,t}(z) \to 0$ due to statistical homogeneity in x and y. The simulations by Hartlep *et al.* (2003) (for $Ra \leq 1 \times 10^7$) also showed that the mean flow contained very little kinetic energy, but De *et al.* (2018) found a long-time periodicity in the mean flow for low Rayleigh numbers, $Ra \leq 2 \times 10^6$.

Rather than having a mean-flow profile with small velocity fluctuations, we are faced with small mean velocity amplitudes in the presence of velocity fluctuations that are up to 2 orders of magnitude larger when the statistics are taken over finite time intervals τ_{total}, as seen from comparisons of table 2 with the data in figure 5. This central result also holds when the aspect ratio of the simulation is varied. It is our view that fluctuations will be relevant for all configurations which includes closed cells of $\Gamma \lesssim 1$, see e.g. figure 9. But their relevance is strongest in the statistically homogeneous plane layer with periodic boundary conditions in the horizontal direction – the configuration that comes closest to the original physical problem of turbulent convection (Spiegel 1962), as relevant for most geo- and astrophysical applications.

We also showed that the corresponding shear Reynolds numbers, which are based on mean-flow quantities for a finite averaging time, remain very small because the characteristic velocities U_∞ are small. The strong fluctuations cause the fluctuation thicknesses of temperature and velocity (defined as the near-wall maxima of the root-mean-square profiles) to differ by an order of magnitude for the highest Rayleigh numbers, as summarized in table 3. This difference increases with Rayleigh number (although the Prandtl number is held fixed at order unity); it becomes particularly pronounced for $Ra \geq 10^9$, a range beyond which previous larger-aspect-ratio DNS studies rarely advanced.

Furthermore, our analysis revealed that the velocity boundary region in the present configuration is a carpet of differently oriented time-dependent and shear-dominated (coherent) regions interspersed by regions of incoherent flow. The latter regions occupy approximately 60 % of the plate area for all Rayleigh numbers. This heterogeneous composition crystallizes particularly for $Ra \gtrsim 10^9$, underlying again the importance of DNS with larger aspect ratios and high Rayleigh numbers. The incoherent regions in the present flow can be as large as the entire cross-section of a cylindrical cell at $\Gamma \sim 1$.

https://doi.org/10.1017/jfm.2024.853 Published online by Cambridge University Press

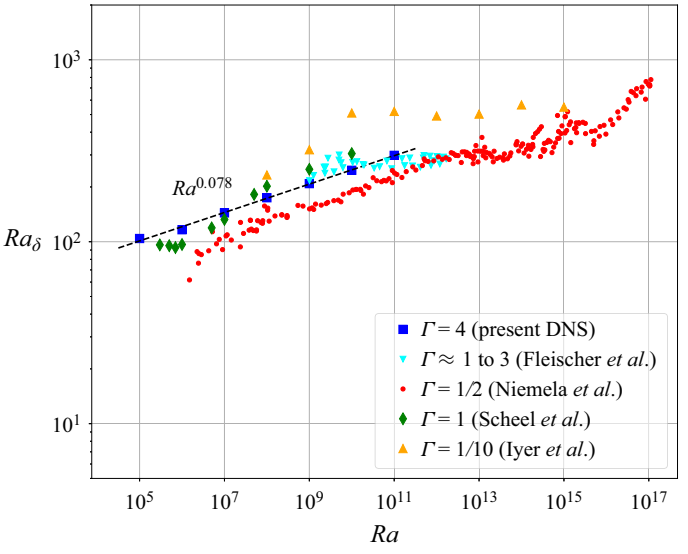

Figure 10. Boundary layer thickness-based Rayleigh number Ra_δ vs Rayleigh number Ra. We have collected for comparison data from other simulations including Scheel & Schumacher (2017) and Iyer *et al.* (2020); also plotted are experimental data from Fleischer & Goldstein (2002) and Niemela *et al.* (2000). Note that all listed data from previous sources use $\delta_T = 1/(2Nu)$ to calculate the boundary layer thickness-based Rayleigh number Ra_δ. Only the present data use $\delta_{T,rms}$ for the determination of Ra_δ. The corresponding Rayleigh numbers $Ra_\delta = Ra_{\delta,rms}$ are found in table 1.

The coherent regions are the near-wall footprint of the circulation rolls which form the large-scale turbulent superstructure pattern (Pandey *et al.* 2018; Stevens *et al.* 2018). They change their orientation continually and thus result in a net zero mean flow, as stated above.

Finally, we showed that the velocity fluctuation thicknesses decrease when they are conditioned on shear-dominated patches in the near-wall region. They are then closer to those scales which are obtained in turbulent convection in closed cylindrical cells of aspect ratio $\Gamma \lesssim 1$. The geometry of the closed cell enforces a LSC which is mostly shear dominated in the vicinity of the walls, as already shown in Schumacher *et al.* (2016), where the time dependence of the orientation has been eliminated. This causes smaller velocity thickness scales that are, however, still larger than the thermal boundary layer thickness at $Pr \sim 1$. Nevertheless, the fluctuation thickness is the consistently definable velocity boundary layer scale for the present turbulent convection flow.

The present results also raise many questions on the possible transition mechanisms of the boundary layer to a turbulent regime and the possible consequences for the global heat transfer. Differently from wall-bounded shear flows, we detect velocity fluctuations everywhere, even though at different strengths; see again figure 9. Furthermore, we do not observe a Rayleigh-number dependence of the ratio of coherent ('laminar') to incoherent ('turbulent') regions. The time scales, at which these complex spatio-temporal patterns change, become increasingly shorter with increasing Rayleigh number. A variation of the threshold for the decomposition into coherent and incoherent boundary regions practically did not affect this Rayleigh-number independence.

The spatio-temporal heterogeneity of the velocity boundary layer, which we detected here, suggests to us the prevalence of local, rather than global, instability mechanisms, which would bring us back to the marginal stability concept of the boundary layer, see e.g. Howard (1966) and for a detailed boundary layer model with plume formation, Theerthan

https://doi.org/10.1017/jfm.2024.853 Published online by Cambridge University Press

& Arakeri (1998). However, figure 10 shows a power-law fit of $Ra_{\delta,rms} = ARa^{\gamma}$ with a very small exponent $\gamma = 0.077$ and $A \approx 41$. The resulting $Ra_{\delta,rms}$ are, by at least a factor of 4, smaller than Howard's critical Rayleigh number of $Ra_{\delta} \sim O(10^3)$. Additional data from experiments show that, even at $Ra \sim 10^{17}$, a thickness-based Rayleigh number Ra_{δ} barely reaches a value of 10^3. This challenges the original marginal stability concept. This question and higher Rayleigh-number simulation in the present configuration form the subject of further study.

Acknowledgements. The authors thank J. Arakeri, B. Hof, H. Nagib and P. Schmid for helpful discussions.

Funding. The work of R.J.S. is funded by the European Union (ERC, MesoComp, 101052786). Views and opinions expressed are, however, those of the authors only and do not necessarily reflect those of the European Union or the European Research Council. The work of JDS was supported by a Mercator Fellowship of the Deutsche Forschungsgemeinschaft within the Priority Programme DFG-SPP 1881 on Turbulent Superstructures. The authors gratefully acknowledge the Gauss Centre for Supercomputing e.V. (https://www.gauss-centre.eu) for funding the project nonbou by providing computing time through the John von Neumann Institute for Computing (NIC) on the GCS Supercomputer JUWELS Booster at Jülich Supercomputing Centre (JSC).

Declaration of interests. The authors report no conflict of interest.

Data availability statement. The data that support the findings of this study are available on reasonable request.

Author ORCIDs.
Roshan J. Samuel https://orcid.org/0000-0002-1280-9881;
Mathis Bode https://orcid.org/0000-0001-9922-9742;
Janet D. Scheel https://orcid.org/0000-0002-1669-4188;
Katepalli R. Sreenivasan https://orcid.org/0000-0002-3943-6827;
Jörg Schumacher https://orcid.org/0000-0002-1359-4536.

Author contributions. All authors designed the research. R.J.S., M.B. and J.S. carried out the supercomputer simulations. R.J.S., J.D.S and J.S. analysed the simulation data and generated the figures. All authors wrote the manuscript.

References

Ahlers, G., Bodenschatz, E., Funfschilling, D. & Hogg, J. 2009*a* Turbulent Rayleigh–Bénard convection for a Prandtl number of 0.67. *J. Fluid Mech.* **641**, 157–167.

Ahlers, G., Grossmann, S. & Lohse, D. 2009*b* Heat transfer and large scale dynamics in turbulent Rayleigh–Bénard convection. *Rev. Mod. Phys.* **81**, 503–537.

Castaing, B., Gunaratne, G., Heslot, F., Kadanoff, L.P., Libchaber, A., Thomae, S., Wu, X.-Z., Zaleski, S. & Zanetti, G. 1989 Scaling of hard thermal turbulence in Rayleigh–Bénard convection. *J. Fluid Mech.* **204**, 1–30.

Chavanne, X., Chillà, F., Castaing, B., Hebral, B., Chabaud, B. & Chaussy, J. 1997 Observation of the ultimate regime in Rayleigh–Bénard convection. *Phys. Rev. Lett.* **79** (19), 3648–3651.

Chillà, F. & Schumacher, J. 2012 New perspectives in turbulent Rayleigh–Bénard convection. *Eur. Phys. J.* E **35**, 58.

Creyssels, M. & Martinard, D. 2024 Stability analysis of sheared thermal boundary layers and its implication for modelling turbulent Rayleigh–Bénard convection. *Eur. J. Mech. (*B*/Fluids)* **105**, 97–103.

De, A.K., Eswaran, V. & Mishra, P.K. 2018 Dynamics of plumes in turbulent Rayleigh–Bénard convection. *Eur. J. Mech. (*B*/Fluids)* **72**, 164–178.

Fischer, P.F., *et al*. 2022 NekRS, a GPU-accelerated spectral element Navier–Stokes solver. *Parallel Comput.* **114**, 102982.

Fleischer, A.S. & Goldstein, R.J. 2002 High-Rayleigh-number convection of pressurized gases in a horizontal enclosure. *J. Fluid Mech.* **469**, 1–12.

https://doi.org/10.1017/jfm.2024.853 Published online by Cambridge University Press

HARTLEP, T., TILGNER, A. & BUSSE, F.H. 2003 Large scale structures in Rayleigh–Bénard convection at high Rayleigh numbers. *Phys. Rev. Lett.* **91**, 064501.

HOF, B. 2022 Directed percolation and the transition to turbulence. *Nat. Rev. Phys.* **5**, 62–72.

HOWARD, L.N. 1966 Convection at high Rayleigh number. In *Applied Mechanics, 11th Congress of Applied Mechanics, Munich* (ed. H. Goertler), pp. 1109–1115. Springer-Verlag Berlin.

IYER, K.P., SCHEEL, J.D., SCHUMACHER, J. & SREENIVASAN, K.R. 2020 Classical 1/3 scaling of convection holds up to $Ra = 10^{15}$. *Proc. Natl Acad. Sci. USA* **117**, 7594–7598.

KADANOFF, L.P. 2001 Turbulent heat flow: structures and scaling. *Phys. Today* **54**, 34–39.

KERR, R.M. 1996 Rayleigh number scaling in numerical convection. *J. Fluid Mech.* **310**, 139–179.

LINDBORG, E. 2023 Scaling in Rayleigh–Bénard convection. *J. Fluid Mech.* **956**, A34.

NIEMELA, J.J., SKRBEK, L., SREENIVASAN, K.R. & DONNELLY, R.J. 2000 Turbulent convection at very high Rayleigh numbers. *Nature* **404**, 837–840.

NIEMELA, J.J. & SREENIVASAN, K.R. 2006 Turbulent convection at high Rayleigh numbers and aspect ratio 4. *J. Fluid Mech.* **557**, 411–422.

PANDEY, A., SCHEEL, J.D. & SCHUMACHER, J. 2018 Turbulent superstructures in Rayleigh–Bénard convection. *Nat. Commun.* **9**, 2118.

RAYLEIGH, LORD 1916 LIX. On convection currents in a horizontal layer of fluid, when the higher temperature is on the under side. *Phil. Mag.* **32**, 529–546.

VAN REEUWIJK, M., JONKER, H.J.J. & HANJALIĆ, K. 2008*a* Wind and boundary layers in Rayleigh–Bénard convection. I. Analysis and modeling. *Phys. Rev.* E **77**, 036311.

VAN REEUWIJK, M., JONKER, H.J.J. & HANJALIĆ, K. 2008*b* Wind and boundary layers in Rayleigh–Bénard convection. II. Boundary layer character and scaling. *Phys. Rev.* E **77**, 036312.

SCHEEL, J.D. & SCHUMACHER, J. 2017 Predicting transition ranges to fully turbulent viscous boundary layers in low Prandtl number convection flows. *Phys. Rev. Fluids* **2**, 123501.

SCHLICHTING, H. & GERSTEN, K. 2016 *Boundary-Layer Theory*. Springer.

SCHUMACHER, J., BANDARU, V., PANDEY, A. & SCHEEL, J.D. 2016 Transitional boundary layers in low-Prandtl-number convection. *Phys. Rev. Fluids* **1** (8), 084402.

SCHUMACHER, J. & SCHEEL, J.D. 2016 Extreme dissipation event due to plume collision in a turbulent convection cell. *Phys. Rev.* E **94**, 043104.

SHI, N., EMRAN, M.S. & SCHUMACHER, J. 2012 Boundary layer structure in turbulent Rayleigh–Bénard convection. *J. Fluid Mech.* **706**, 5–33.

SHISHKINA, O. & LOHSE, D. 2023 Ultimate turbulent thermal convection. *Phys. Today* **76**, 26–32.

SPIEGEL, E.A. 1962 On the Malkus theory of turbulence. In *Mécanique de la Turbulence* (ed. Centre National de la Recherche Scientifique (CNRS)). pp. 181–201.

SREENIVASAN, K.R., BERSHADSKII, A. & NIEMELA, J.J. 2002 Mean wind and its reversal in thermal convection. *Phys. Rev.* E **65**, 056306.

STEVENS, R.J.A.M., BLASS, A., ZHU, X., VERZICCO, R. & LOHSE, D. 2018 Turbulent thermal superstructures in Rayleigh–Bénard convection. *Phys. Rev. Fluids* **3**, 041501(R).

STEVENS, R.J.A.M., LOHSE, D. & VERZICCO, R. 2011 Prandtl and Rayleigh number dependence of heat transport in high Rayleigh number thermal convection. *J. Fluid Mech.* **688**, 31–43.

STEVENS, R.J.A.M., VERZICCO, R. & LOHSE, D. 2010 Radial boundary layer structure and Nusselt number in Rayleigh–Bénard convection. *J. Fluid Mech.* **643**, 495–507.

THEERTHAN, S.A. & ARAKERI, J. 1998 A model for near-wall dynamics in turbulent Rayleigh–Bénard convection. *J. Fluid Mech.* **373**, 221–254.

URBAN, P., HANZELKA, P., KRALIK, T, MUSILOVÁ, V., SRNKA, A. & SKRBEK, L. 2012 Effect of boundary layers asymmetry on heat transfer efficiency in turbulent Rayleigh–Bénard at very high Rayleigh numbers. *Phys. Rev. Lett.* **109**, 154301.

VERMA, M.K. 2018 *Physics of Buoyant Flows: From Instabilities to Turbulence*. World Scientific.

WU, X.Z. & LIBCHABER, A. 1992 Scaling relations in thermal turbulence: the aspect ratio dependence. *Phys. Rev.* A **45**, 842–845.

ZAHTILA, T., LU, W., CHAN, L. & OOI, A. 2023 A systematic study of the grid requirements for a spectral element solver. *Comput. Fluids* **251**, 105745.

https://doi.org/10.1017/jfm.2024.853 Published online by Cambridge University Press